

Efficient Synthesis of $\text{WB}_{5-x}-\text{WB}_2$ Powders with Selectivity for WB_{5-x} Content

Alexander Ya. Pak, Dmitry V. Rybkovskiy, Yuliya Z. Vassilyeva, Ekaterina N. Kolobova, Alexander V. Filimonenko, and Alexander G. Kvashnin*



Cite This: <https://doi.org/10.1021/acs.inorgchem.1c03880>



Read Online

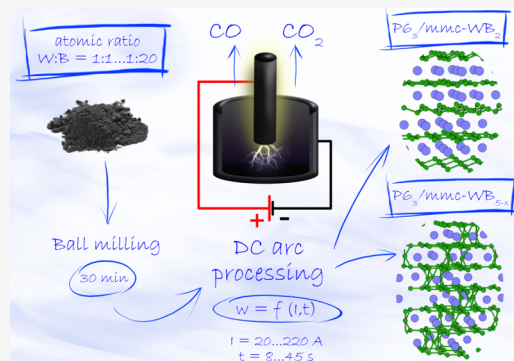
ACCESS |

Metrics & More

Article Recommendations

Supporting Information

ABSTRACT: We proposed an efficient method toward the synthesis of higher tungsten boride WB_{5-x} in the vacuumless direct current atmospheric arc discharge plasma. The crystal structure of the synthesized samples of boron-rich tungsten boride was determined using computational techniques, showing a two-phase system. The ab initio calculations of the energies of various structures with similar X-ray diffraction (XRD) patterns allowed us to determine the composition of the formed higher tungsten boride. We determined the optimal parameters of synthesis to obtain samples with 61.5% WB_{5-x} by volume. The transmission electron microscopy measurements showed that 90% of the particles have sizes of up to 100 nm, whereas the rest of them may have sizes from 125 to 225 nm. Our study shows the possibility of using the proposed vacuumless method as an efficient and inexpensive way to synthesize superhard WB_{5-x} without employing resource-consuming vacuum techniques.



INTRODUCTION

A large number of higher tungsten borides have attracted the attention of scientists due to their high hardness, thermal resistance, low thermal conductivity, catalytic activity, etc.^{1–10} Wide regions of homogeneity of W–B phases^{1–3,11–13} may be caused, at least partly, by extensive polysomatism,¹⁴ which leads to significant difficulties in synthesizing single crystals with a well-defined structure and stoichiometry. There are five stable tungsten boride phases known and well-studied by experiments, namely, W_2B ,^{11,15} WB (including α and β phases),^{15,16} WB_2 ,¹⁷ and WB_4 .¹⁸ The most intriguing story is related to the crystal structure determination of the higher tungsten boride that was previously determined as WB_4 ,^{7,11,18–20} W_{2-x}B_9 ,²¹ WB_{12} ,²² W_{1-x}B_3 ,^{23,24} and $\text{WB}_{4,2}$.²⁵ Recent theoretical and experimental studies^{1,3} have shown that this higher tungsten boride has a disordered structure and, because of broad homogeneity, a WB_{5-x} composition. Various experimental techniques have been used to characterize samples of higher tungsten borides.^{20,23,25} This material as well as other refractory metal borides can be easily synthesized by applying traditionally used techniques, namely, high-temperature sintering, spark plasma sintering, etc.^{3,7,25,26} Recently,³ hard compacts based on a mixture of WB_{5-x} and WB_2 with a high content of WB_{5-x} (from 75 to 95%) were obtained at a pressure of 1.5 GPa and temperatures of 1100–1300 °C from a nanometer-sized powder mixture of tungsten and boron. Study of mechanical properties of WB_{5-x} showed the clear possibility of it being used in drill bit cutters for oil and gas production with measured hardness, which is 30–50%

higher than that of the hard alloy 94WC–6Co.³ The main disadvantage of all mentioned methods is the requirement of a vacuum or an inert atmosphere (i.e., high-purity argon) during the synthesis, which increases the production cost and limits the production itself. Thus, it is highly required to find an efficient way for large-scale synthesis of this material as it is a very promising candidate for the drilling technology instead of WC-based hard alloys.

The main goal of this work is to develop new ways of efficient and inexpensive synthesis of a hard and economically interesting material. In this research, we proposed and investigated a new experimental method of synthesis of WB_{5-x} using a vacuumless technique proposed by Pak et al.^{27,28} We optimized the parameters of the synthesis to obtain $\text{WB}_{5-x}-\text{WB}_2$ samples containing over 60% of WB_{5-x} by volume displaying high hardness.

EXPERIMENTAL SECTION

Synthesis. The synthesis of single crystals of higher tungsten borides was carried out on a laboratory bench by heating a mixture of reagents by an electric arc plasma in a self-shielded autonomous gas medium.²⁷ Here, we avoid the use of a vacuum, which makes this

Received: December 13, 2021

method more preferable for further use in large-scale production. We used graphite electrodes, where the anode was a rod with a diameter of 8 mm and the water-cooled cathode was a crucible. The initial raw powder was compacted with a load of 1 kg using a graphite rod (all images are shown in Figure S1 in the Supporting Information).

To perform the fine control of the parameters and increase the repeatability of the experiments, we used specially developed software for this experimental equipment. The automated electric drive based on a bipolar stepper motor provides regulation of the size of the discharge gap and stabilizes the discharge. The power supply control system provides a repeatable current–voltage characteristic curve of the discharge. The accuracy of regulation of the size of the discharge gap is not less than 0.1 mm, which is especially important under conditions of anode consumption. Even though the process is characterized by high heating dynamics, a high temperature gradient, and the presence of random factors (statistical variation of parameters), the experiments are reproducible due to exclusion of a human factor from the working cycle. The validity of application of such a procedure is confirmed by the patents obtained for the experimental setup and software.^{29,30}

The powders of amorphous boron (MC MINTS MATERIALS Ltd., 99.9% purity) and metallic tungsten (obtained from the Faculty of Chemistry of Tomsk Polytechnic University using the method of electric explosion of conductors, 99.9% purity) were mixed in a ball mill in zirconium dioxide dishes with zirconium dioxide balls (5 mm in diameter) for 30 min. The ratio of balls to raw material masses was ~1:8. The mixture was placed at the bottom of a crucible.

The experiments were performed in three series. In the first series, the powder mixture with an atomic ratio of W/B varying from 1:1 to 1:20 was heated by an electric arc with a current of 220 A for 45 s. In the second series, the atomic W/B ratio was 1:15, the electric current was 220 A, and the arc durations were 8, 15, 25, 35, and 45 s. In the third series, the atomic W/B ratio was 1:15, the currents of the electric arc were 20, 60, 110, 160, and 220 A, and the heating was performed for 25 s. In these series of experiments, the mass of the initial powder was 1 g, while the influence of the mass on the composition of the product was studied separately in the fourth series of experiments, where the masses of the initial mixture of powders were 0.5, 1.0, 1.5, 2.0, and 2.5 g with a fixed atomic W/B ratio of 1:15, a current of the electric arc of 60 A, and a duration time of 25 s.

In the first series of experiments, the atomic ratio was varied from 1:1 to 1:20 to synthesize lower and higher tungsten borides in the condition of a high boron excess, which was several times higher than in the synthesis of WB_{5-x} .³ The electric current of 220 A was the maximum for this experimental setup. The arc duration of 45 s was chosen to bring the system to a steady-state thermal condition: a longer duration does not lead to an increase in the electrode temperature measured on the outer wall of the cathode. The subsequent series of experiments attempted to reduce the energy input, and indirectly the temperature, by reducing the duration and electric current of the arc.

Characterization and Analysis. The obtained samples were extracted from the graphite crucible and crushed in an agate mortar. The X-ray phase analysis was carried out using a Shimadzu XRD 7000s X-ray diffractometer (Cu-K α irradiation with a graphite monochromator with $\lambda = 1.54060 \text{ \AA}$), with the angle 2θ ranging from 10 to 90°. The quantitative analysis and the quantitative estimation of the phase ratio in the product were performed by the integrated intensity of the diffraction maxima, described in ref 31, which is a standard approach for the analysis of X-ray diffraction (XRD) patterns. Additionally, we calculated the phase ratio in the product using the reference intensity ratio (RIR) method, which is described in refs 32 and 33. The difference/deviation of the calculated values by the two methods was not more than 10%; the detailed information is presented in the Table S2, Supporting Information.

Scanning electron microscopy (SEM) was carried out using a Tescan Vega 3 SBU microscope equipped with an energy-dispersive analyzer attachment Oxford X-Max-50 with a Si/Li crystal detector.

Transmission electron microscopy (TEM) was carried out using a JEOL JEM2100F microscope. During the sample preparation, the

nanoscale fraction was isolated by treating powders in an alcohol suspension in an ultrasonic bath and applied to a standard carbon amorphous substrate on a copper grid. The analysis of the obtained images was made using Gatan DigitalMicrograph ver. 1.80.70.

The differential thermal analysis was carried out using the Netzsch STA 449 Jupiter thermal analyzer in an oxidizing environment at temperatures from room temperature to 1200 °C.

The surface elemental composition and chemical/electronic states of atoms on the surfaces of WB, WB_2 , and two samples of $\text{WB}_{5-x}-\text{WB}_2$ with different amounts of the WB_{5-x} phase were determined by X-ray photoelectron spectroscopy (XPS) using an ultrahigh vacuum photoelectron spectrometer Thermo Scientific K-Alpha Nexsa. An X-ray tube with an aluminum anode was used to excite monochromatized X-rays (1486.74 eV). The survey and high-resolution spectra of individual elements were recorded at 200 and 50 eV with steps of 1 and 0.1 eV, respectively. The binding energy (BE) was calibrated using the main C 1s peak with a binding energy (BE) of 285.0 eV. The obtained spectra were processed using Avantage Thermo Fisher and CasaXPS software.

Hardness Measurements. The mechanical properties of synthesized materials based on WB_{5-x} and WC were investigated via microindentation using a Dynamic Ultra Micro Hardness Tester (DUH-211, Shimadzu) with a load range of 0.1–1 N with a dwell time of 10 s. Before the measurements, the special preparation of the sample was made. Powder samples were poured into a cylindrical mold with an inner diameter of 20 mm and poured with epoxy resin. Sample preparation of the poured powders was carried out using a grinding and polishing machine EcoMet 300 PRO with a semi-automatic nozzle AutoMet 300 PRO (Buehler). SiC sandpaper was used during the grinding, and polishing was performed using diamond polycrystalline suspensions.

Indentation was performed on particles with a size of several tens of micrometers. The primary data were automatically processed using the built-in hardness tester software. Measured Vickers microhardness values under applied loads of 0.5 and 1 N were verified by size of the indenter imprint. Under each load, the surface was indented at 15 randomly chosen spots to ensure very accurate hardness measurements.

To clarify the data on the hardness of our samples, large pieces of synthesized materials with sizes of several millimeters were selected from the sample with the highest content of the WB_{5-x} phase. The samples were poured into special metallographic epoxy compounds (Technovit 5000) and, after their hardening, were subjected to a thorough surface treatment during grinding on diamond 320, 600, 800, and 1200 papers on a Forcipol 300 1V machine. Polishing was carried out on polishing fabrics of 6, 3, 1, and 0.25 μm using appropriate diamond suspensions on the same equipment. Each stage was accompanied by a thorough surface cleaning to eliminate the presence of impurities, which can influence the results.

Computational Details. Our calculations were based on the density functional theory (DFT)^{34,35} within the generalized gradient approximation (the Perdew–Burke–Ernzerhof functional)³⁶ and the projector augmented wave method,^{37,38} as implemented in the VASP^{39–41} code. The plane-wave energy cutoff of 400 eV, the Methfessel–Paxton smearing⁴² of electronic occupations, and Γ -centered k -point meshes with a resolution of $2\pi \times 0.025 \text{ \AA}^{-1}$ for the Brillouin zone sampling were used, ensuring convergence of the energy differences and stress tensors. Stability at finite temperatures was studied using the calculations of the Helmholtz free energy

$$F(T) = E_0(V) + F_{\text{vib}}(V, T) \quad (1)$$

where E_0 is the total energy from the DFT calculations and F_{vib} is the vibrational Helmholtz free energy calculated from the following relation in the harmonic approximation⁴³

$$\begin{aligned} F_{\text{vib}}(V, T) &= k_B T \int_{\Omega} g(\omega(V)) \ln \left[1 - \exp \left(-\frac{\hbar \omega(V)}{k_B T} \right) \right] d\omega \\ &\quad + \frac{1}{2} \int g(\omega(V)) \hbar \omega d\omega \end{aligned} \quad (2)$$

Here, $g(\omega(V))$ is the phonon density of states at the given volume, calculated using the finite displacement method as implemented in PHONOPY,^{44,45} with forces computed using VASP,^{39–41} k_B is the Boltzmann constant; and ω is the phonon frequency.

The crystal structures of possible polymorphic modifications of W_2B_5 were predicted using the first-principles fixed-composition evolutionary algorithm search as implemented in the USPEX code.^{46–48} During the structure search, the first generation of 160 structures was produced randomly with up to 48 atoms in the primitive unit cell. The succeeding generations were obtained by applying the heredity (40%), softmutation (20%), and transmutation (20%) operators; 20 and 15% of each generation were produced using the random symmetric⁴⁹ and random topological generators,⁵⁰ respectively.

RESULTS AND DISCUSSION

Experimental Setup. To perform synthesis of higher tungsten boride, we developed an experimental setup of a vacuumless method of synthesis, whose principal scheme is illustrated in Figure 1. The distinctive feature of the proposed

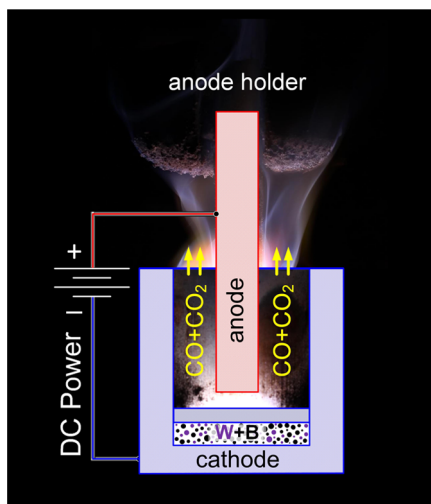


Figure 1. Schematic illustration of the experimental setup with denoted main parts of the arc reactor.

method is the realization of the synthesis process in an open-air environment, which simplifies the design of the electric arc reactor by eliminating the vacuum chamber, pumps, and gas distribution equipment, which leads to a several-fold increase in the energy efficiency of the synthesis process. Synthesis of various materials, including tungsten borides, is possible due to the intensive generation of protective CO and CO₂ gases resulting from the interaction of eroded carbon from the electrodes with air oxygen and shielding the reaction zone from oxidation. The special design of the electrode system makes it possible to minimize the presence of eroded carbon from the anode in the synthesis product, which is also a significant advantage over analogues. Thus, the performed series of experiments showed that carbon coming from graphite electrodes that goes into products was identified in insignificant amounts.

During the work of the arc reactor, the processes of heat and mass transfer occur between the components of the experimental system. The electrodes lose their mass during the work of the arc reactor. As a result of the electrical erosion process, part of the mass of the anode is transferred to the cathode to form a cathode deposit. Both the anode and the

cathode can also lose mass because of oxidation processes with the formation of CO and CO₂ gases. These gases form an autonomous gas environment of the synthesis process.

It was found that the mass of the cathode changes insignificantly during the synthesis ($\Delta m_{\text{cathode}}$ not more than 0.1 g, which is about 1%). The mass of the anode changes depending on the parameters of the synthesis process. In the series, with an increase in the arc duration of the powder mixture by electric arc plasma from 8 to 45 s, Δm of the anode changes from 0.22 to 0.64 g due to intensive electrical erosion processes on increasing the amount of electrical energy transmitted through the electrodes. Change in the current from 20 to 220 A leads to changes in Δm_{anode} from 0.01 to 0.7 g. The amount of supplied energy to the initial mixture of the powder in the series with the W/B ratio varying from 1:1 to 1:20 at the current of 220 A and an arc duration of 45 s was about 270 ± 10 kJ. On increasing the fusion time from 8 to 45 s (at the current strength of 220 A), the amount of supplied energy changed from 50 to 270 kJ, whereas an increase in the current from 20 to 220 A with an arc duration of 25 s leads to changes in the supplied energy from 19 to 163 kJ. The average power of the arc discharge in the series on changing the current was from 0.74 to 6.52 kW, and the average power in all other experiments (with the current of 220 A) was 6.0 ± 0.5 kW.

Synthesis. The powder X-ray diffraction (XRD) patterns of the compounds synthesized in the first series of experiments are shown in Figure 2. The sample obtained from the powder with the ratio W/B = 1:1 contains two phases, the majority of which can be identified as α -WB with the space group $I4_1/amd$ (Figure 2a). Other diffraction peaks belong to $I4/m$ -W₂B, marked by triangles in Figure 2a. Formation of the main WB phase is essential, considering the atomic ratio W/B = 1:1 in the initial mixture and the conditions of sufficient energy input in the reaction zone leading to the required temperature. Formation of W₂B can be caused by local inhomogeneities in the chemical distribution during the synthesis and by partial evaporation of boron during the plasma treatment, resulting in a local excess of tungsten, or deficiency of boron.

Changes in the tungsten–boron ratios to 1:3 and 1:5 lead to the formation of $P6_3/mmc$ -WB₂ as the main phase, marked by rhombuses in Figure 2a. Further increase in the boron concentration to W/B = 1:10 leads to the formation of $P6_3/mmc$ -WB_{5-x}, marked by circles in Figure 2a. The experimental data with changes in boron content is summarized in Figure 2b. The highest amount of WB_{5-x} was observed for W/B = 1:15. The volume of the reaction zone does not allow us to increase the boron concentration to more than W/B = 1:20. The amount of higher tungsten boride WB_{5-x} rises from ~12 to 15% by volume as the W/B atomic ratio changes from 1:10 to 1:20; for W/B = 1:15 and 1:20, the sample compositions are very close to each other (Figure 2b). The formation of the highest boride WB_{5-x} in plasma requires a significant excess of boron—at least W/B = 1:10. An increase in the boron content past W/B = 1:15 does not lead to a rise in the amount of WB_{5-x} in the sample (Figure 2a,b). Therefore, further experiments were performed with W/B = 1:15.

Interpretation of the Crystal Structure of Synthesized Phases. The obtained samples have a complex XRD pattern containing two phases, which we identified. The main diffraction peaks at 19.7, 24.2, 28.2, and 34.5° belong to higher tungsten boride WB_{5-x}, which has been synthesized recently.³ The simulated XRD pattern of WB_{5-x} compared

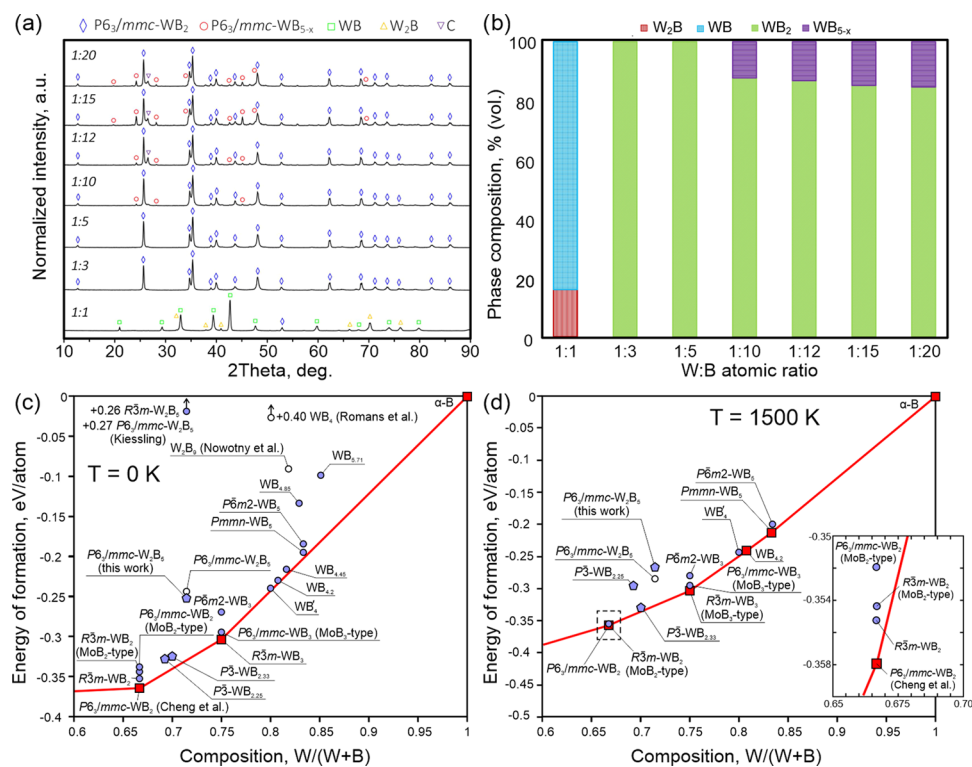


Figure 2. (a) X-ray powder diffraction patterns of the synthesized samples with different tungsten–boron atomic ratios in the initial mixture. (b) Quantitative X-ray diffraction analysis of the synthesized samples in the series of experiments with varied W/B atomic ratios. Calculated boron-rich part of the W–B system convex hull at (c) 0 K and (d) 1500 K. Red squares indicate stable phases; pentagons, stars, and circles designate metastable ones.

with the experimental data is shown in the Figure S2, Supporting Information. Initially, the second phase can be interpreted as W₂B₅,¹⁵ whose XRD pattern perfectly describes the experimental diffraction peaks at 12.7, 19.7, 25.7, and 35.5°. Traces of graphite, the material of the discharge circuit electrodes, were also observed in the obtained XRD pattern, with the main peak at 26.4°.

Two polymorphic modifications of the W₂B₅ phase have been mentioned in the literature.² Structures with space groups P₆₃/mmc and R₃m have been proposed by Kiessling,¹⁵ however, the existence of R₃m has been questioned in experiments.¹² Theoretical studies have shown that the lowest-energy modification has the space group P₆₃/mmc.^{2,51}

To understand which structure best corresponds to the experimental data, we studied the thermodynamical stability of the W–B phases for the W/B ratios from 1:2 to 1:5. The energy–composition phase diagram calculated at 0 K is shown in Figure 2c. We recalculated the energies of both experimentally known and theoretically predicted phases to obtain the most complete picture of stability. The phase P₆₃/mmc-WB₅ is metastable, lying 85 meV/atom above the convex hull, whereas R₃m-WB₅ has a positive formation energy, which agrees with previous theoretical studies.^{2,51} In a fixed-composition evolutionary search using the USPEX code,^{46–48} we predicted the crystal structure of W₂B₅ to have the space group P₆₃/mmc and a lower energy of formation compared to the structure proposed by Kiessling¹⁵ (marked in Figure 2c by a hollow circle and a blue pentagon, respectively, close to each other). The crystal structure of the predicted compound and other crystal data are summarized in the Table S1, Supporting Information.

Considering the similarities between the crystal structures of WB₂ and WB₃, we created new structures with intermediate compositions combining the WB₂- and WB₃-type layers. The obtained structures have compositions WB_{2.25} and WB_{2.33} with global space symmetries P₆₃/mmc and R₃m, respectively (the local symmetry of both phases is P₃). These structures, marked by blue pentagons in Figure 2c lying close to each other, have a relatively low energy of formation at 0 K and are located much closer to the convex hull (16 and 15 meV/atom above it, respectively) than W₂B₅. The convex hull calculated at 2000 K is shown in the Figure S2, Supporting Information.

The XRD patterns of both P₆₃/mmc-WB₂ and P₆₃/mmc-WB₅ well describe the second phase observed in the experimental sample because of similarity of their crystal structures (Figures S3, S4, Supporting Information). Therefore, it is difficult to specify whether WB₂ or W₂B₅ was synthesized. However, the phase diagrams calculated at 0 and 1500 K show that at a high temperature, the thermodynamically stable phase is R₃m-WB₂ having a MoB₂-type structure (Figure 2d). The energy difference between all considered polymorphic modifications of WB₂ is very small (within several meV/atom), which leads to an equal probability for all modifications to be formed during the experiments. Thus, the first-principles calculations together with the simulations of the XRD patterns show that the second phase in our experiments is P₆₃/mmc-WB₂.

Determining the Optimal Parameters of Synthesis of WB_{5-x}. To increase the amount of WB_{5-x} in the sample after choosing the optimal W/B = 1:15 for the synthesis, we varied the electric current, the arc duration, and the mass of the initial powder mixture. The XRD patterns of the synthesized samples obtained with an arc duration of 8–45 s are shown in Figure

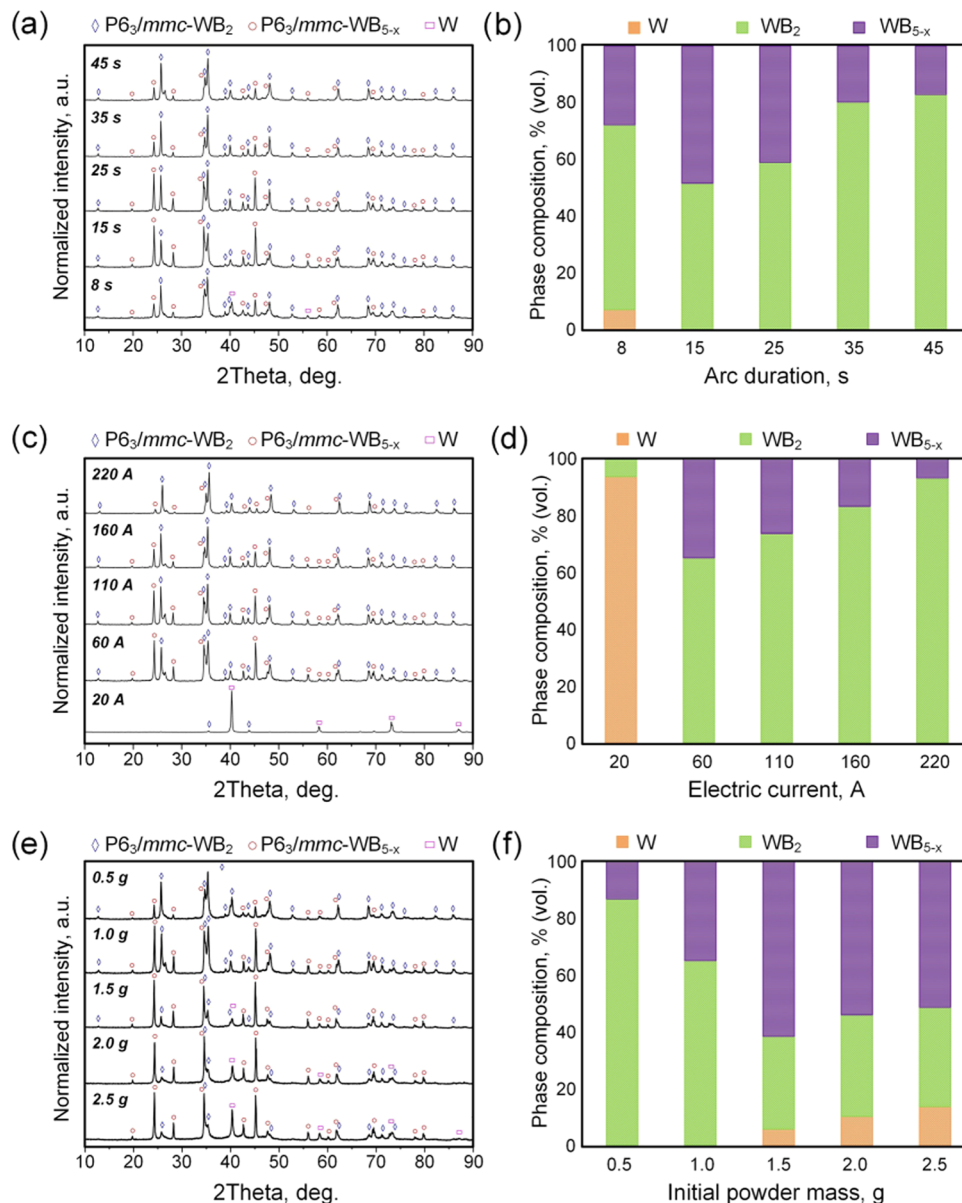


Figure 3. X-ray powder diffraction patterns of the synthesized samples obtained with varied (a) arc durations, (b) electric currents, and (c) initial powder masses. Quantitative X-ray diffraction analysis of the synthesized samples in the series of experiments with varied (d) arc durations, (e) electric currents, and (f) initial powder masses.

3a. In these experiments, W/B = 1:15, the electric current was 220 A, and the mass of the initial powder mixture was 1 g. With an arc duration of 8 s, we obtained cubic tungsten together with WB₂ and WB_{5-x}. The highest diffraction peaks of WB_{5-x} were observed with an arc duration of 15 s. Here the maximum amount of WB_{5-x} in the sample was observed at 15 s (Figure 3b). This time is sufficient to transform the original tungsten and boron powders into higher tungsten boride. With the arc duration increasing further, the amount of WB_{5-x} fell from ~49 to ~17% by volume.

The XRD patterns of the samples obtained with the electric current varying from 20 to 220 A, a fixed W/B ratio, an arc duration of 25 s, and a mass of initial powder mixture of 1 g are shown in Figure 3d. The minimum current of 20 A did not lead to formation of any boride phases; only cubic tungsten was identified in the sample. At this current, the amount of injected energy and resulting thermal field of the arc discharge

are probably insufficient for the formation of tungsten borides. When the current was increased to 60 A, two main phases, WB₂ and WB_{5-x}, were identified in the sample. A further increase in the electric current resulted in lower diffraction peaks of WB_{5-x}. The maximum amount of WB_{5-x} ~35% by volume, was obtained at a current of 60 A with an arc duration of 25 s, W/B = 1:15, and the mass of the initial powder mixture of 1 g. An additional experiment with a current of 60 A and an arc duration of 15 s showed the presence of unreacted tungsten in the products. Thus, further experimental series were performed with an arc duration of 25 s to let the powder warm up and at the same time with successively increased mass of initial mixture of powders.

The XRD patterns of samples obtained from different masses of initial powder are shown in Figure 3e, and the quantitative X-ray diffraction analysis is shown in Figure 3f. One can see that the maximum amount of WB_{5-x} of about

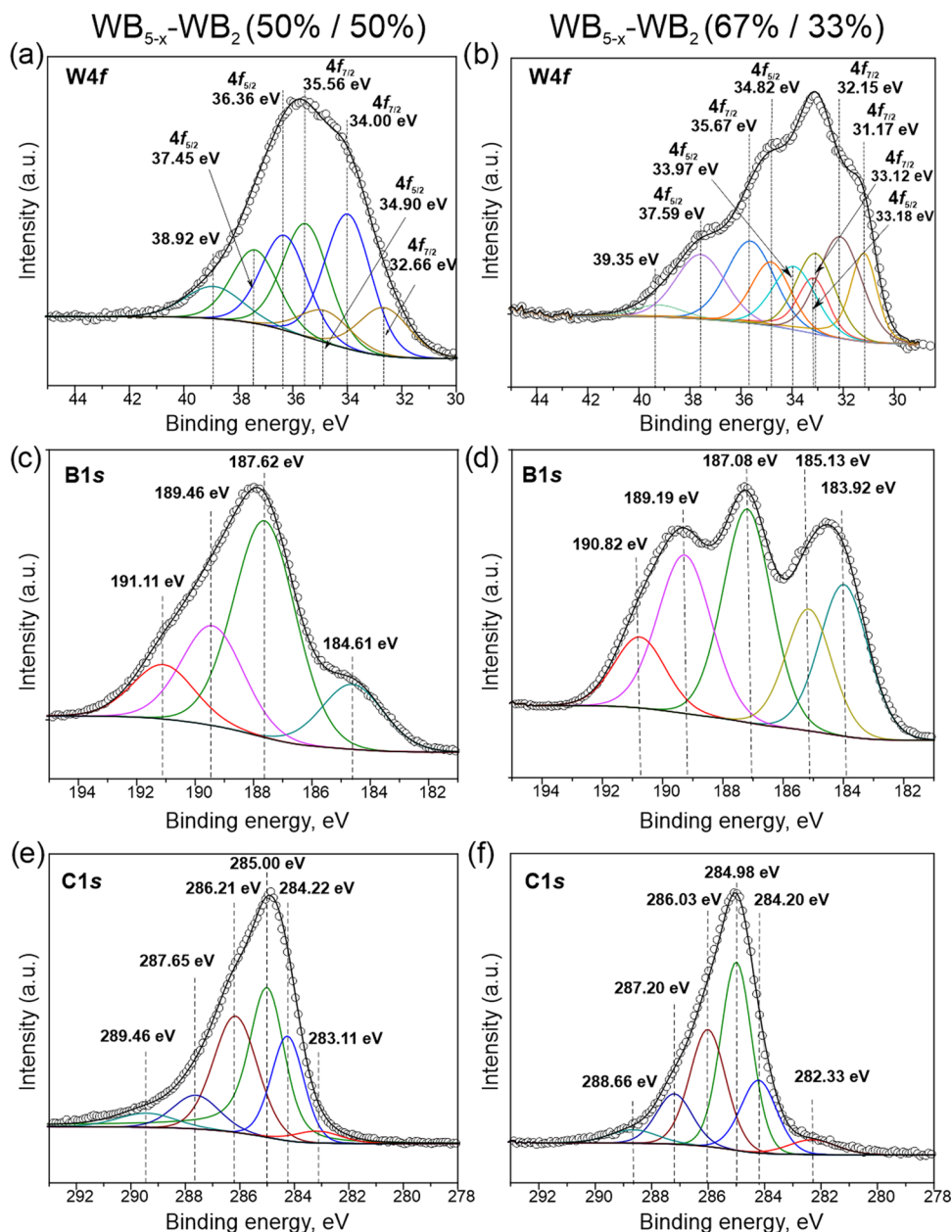


Figure 4. High-resolution XPS spectra for (a, b) W4f, (c, d) B1s, and (e, f) C1s regions of samples containing $\text{WB}_{5-x}\text{-WB}_2$ (50/50%) and $\text{WB}_{5-x}\text{-WB}_2$ (67/33%), respectively.

61.5% in the $\text{WB}_{5-x}\text{-WB}_2$ sample was observed when the mass of the initial powder was 1.5 g. The maximum amount of WB_{5-x} was also estimated using the reference intensity ratio (RIR) method, which gives a higher value of 72.6% by volume (see Table S2 in the Supporting Information). Further increase in the mass leads to a decrease in the amount of WB_{5-x} because the volume of the initial powder cannot be uniformly heated by plasma and most of the powder forms WB_2 instead of WB_{5-x} . For this sample, the relative amount of $\text{WB}_{5-x}/\text{WB}_2$ was 67:33% considering only the higher tungsten boride phase in the sample; the amount of unreacted tungsten was not taken into account as it is less than 5% (see Figure 3b,d,f). Determination of the amount of each higher boride phase in the sample with the largest amount of WB_{5-x} was performed using two methods (Rietveld and RIR), as shown in Table S2 (see the Supporting Information).

Arc discharge experiments with close initial conditions may lead to significantly different results because the parameters of an arc discharge may scatter considerably, which introduces additional possible errors to the known possible errors of the quantitative X-ray phase analysis. Nevertheless, the results of the quantitative composition evaluation (Figure 3d,f) allow us to conclude that the stabilization of WB_{5-x} requires a significant excess of boron, sufficient energy to process the feedstock, and keeping the feedstock energy and temperature in a certain range near the necessary minimum. Larger amounts of input energy and higher temperature lead to decomposition of WB_{5-x} and promote phase transformation into WB_2 . Thus, this method allows one to control the composition of the final product by flexible variation of experimental setup parameters.

It should be noted that neither boron carbide nor tungsten carbide was identified by X-ray diffraction. In the performed

series of experiments, carbon from graphite electrodes that goes into products was identified in insignificant amounts. It is obvious that the initial mixture of powders is in contact with the walls of the cathode (carbon), but the temperature of the cathode wall is much lower than the temperature in the reaction zone due to its cooling. Moreover, the mass of the initial powders and the contact area of tungsten with boron particles is much larger than the contact area with graphite of the cathode walls. Therefore, the possible fraction of boron and tungsten carbides is incommensurably small, so there are no detectable reflections corresponding to boron carbide and/or tungsten carbide phases in the XRD patterns. Another issue that should be noted is that carbon, which is a product of anode erosion (well-known phenomenon), includes in the product of synthesis; carbon is deposited as a solid cathode residue on the sample surface and is removed mechanically from the synthesized sample together with the top layer of the sample, which is the most exposed to the carbon plasma. Due to the high temperature gradient and different thermophysical properties of graphite and synthesis products, the top layer is easily removed mechanically.

The information about the scanning electron microscopy (SEM) investigation of the samples with predominant WB and $WB_{5-x}-WB_2$ phases are presented in the Supporting Information (Figures S5 and S6). We found that samples with the highest amount of WB_{5-x} contain mostly spherical objects with sizes from fractions of a micron to tens of microns (Figure S5 in the Supporting Information), with the composition containing ~90 atom % boron, ~6 atom % tungsten, ~3 atom % oxygen, and ~1 atom % impurities. Transmission electron microscopy analysis was performed for a detailed study of the crystal structure of the obtained samples. The high-resolution TEM (HRTEM) results of the two-phase samples containing WB_2 and WB_{5-x} are shown in Figure S7 in the Supporting Information. The selected area electron diffraction (SAED) pattern (Figure S7b and Table S3 in the Supporting Information) shows the presence of many individual reflections corresponding to WB_2 and WB_{5-x} showing high crystallinity of the obtained compounds. It is important that according to both SEM and TEM analyses the average size of synthesized particles is independent of changes in synthesis parameters (arc duration, current, etc.).

X-ray Photoelectron Spectroscopy. The surface elemental composition was evaluated based on the survey spectra obtained from the studied materials. The following elements were detected for all studied samples: carbon, oxygen, nitrogen, boron, and tungsten. For a more detailed study of the electronic state of the main elements present on the surface, the high-resolution spectra of W4f, B1s, and C1s regions were recorded. XPS spectra of W4f, B1s, and C1s for samples containing WB and WB_2 are presented in Figure S9, along with contributions of electronic states of elements calculated according to XPS for the studied samples containing the maximum amounts of WB, WB_2 , and $WB_{5-x}-WB_2$. Samples were labeled as WB, WB_2 , $WB_{5-x}-WB_2$ (50/50%), and $WB_{5-x}-WB_2$ (67/33%), where the relative ratio of the indicated phases of higher tungsten borides in the sample is written in parentheses. Calculated information is summarized in Tables S5–S7 in the Supporting Information.

Figure 4a,b shows XPS spectra of the W4f region from the samples $WB_{5-x}-WB_2$ (50/50%) and $WB_{5-x}-WB_2$ (67/33%). Tungsten on the surface of the studied samples is in three states for $WB_{5-x}-WB_2$ (50/50%) and four states for WB_{5-x}

WB_2 (67/33%), namely, WO_2 , WB_2 , and WB_3 or $WB_{5-x}WO_3$ with BE(W4f_{7/2}) in the intervals 32.15–32.66, 33.57–34.84, and 35.56–36.16 eV, respectively, as well as an additional state with BE(W4f_{7/2}) in the interval 31.17–31.59 eV allocated only for $WB_{5-x}-WB_2$ (67/33%) and related to the W–W bond.^{52–57} The presence of the latter is confirmed by XRD data for this sample. As it can be seen, the contribution of these states varies depending on the synthesis conditions (current strength, exposure time, etc.), as well as the ratio of reagents (see Table S5 in the Supporting Information). One can note that the surface of samples is partially oxidized (55–57%, Table S5). At the same time, according to XRD data (Figures 2 and 3), the tungsten oxide phases were not detected. Thus, we can assume that the appearance of the W–O bond is due to the interaction of samples with air oxygen during the synthesis/storage/transportation of samples. XPS peaks with binding energies of 33.58–34.83 eV suggest the presence of W–B(III) bonds, indicating the availability of WB_3 or WB_{5-x} phases in our samples (see Figure 4a,b). This can be explained by the fact that the crystal structure of WB_{5-x} is derivative of WB_3 and can be considered as WB_3 with some of the tungsten atoms in the Wyckoff position 2b replaced with three boron atoms arranged in triangles whose plane coincides with that of the tungsten atoms; see ref 3 for details.

The B 1s spectra for $WB_{5-x}-WB_2$ (50/50%) and $WB_{5-x}-WB_2$ (67/33%) were deconvoluted into four and five components, namely, with BE(B 1s) in the interval 183.92–184.61 eV indicating the presence of a B–B bond of amorphous boron; with BE(B1s) in the interval 187.08–187.62 indicating the presence of a W–B bond; with BE(B1s) in the intervals 189.19–189.46 and 190.51–191.11 eV indicating B–O bonds in B_xO_y (see Figure 4c,d and Table S5),^{52,55–64} as well as for the sample of $WB_{5-x}-WB_2$ (67/33%), it was additionally identified the B 1s state with BE in the interval 185.01–186.06 eV related to the B–C bond; see Figure 4d and Table S5 in the Supporting Information. It should be noted that, as in the case of tungsten, the presence of the B–O bond indicates a partial oxidation of the sample surface by atmospheric oxygen. At the same time, as for tungsten, the boron oxide phase was not detected in the X-ray diffraction patterns. In addition, it is worth noting that in the B1s spectrum for $WB_{5-x}-WB_2$ (67/33%), a state with BE corresponding to the B–C bond was identified, in contrast to the spectrum of W4f where this state was not detected. The reason for this may be that an excess of boron was used in the synthesis as compared to tungsten.

Figure 4e,f shows the XPS spectra of the C1s region. The experimental curve for the investigated materials can be deconvoluted into six separate components, indicating the presence of the following bonds: W–C, B–C, C–C, C–OH, O–C–O, and O–C=O with binding energy in the intervals 282.33–283.11, 284.20–284.26, 284.82–285.02, 285.54–286.21, 286.79–287.65, and 288.33–289.46 eV, respectively.^{52,53,58–64} There are no significant differences in C 1s XPS spectra of samples containing either $WB_{5-x}-WB_2$ or WB and WB_2 ; see Figures 4e,f and S9 in the Supporting Information. The main contribution corresponding to the C–C bond comes from the graphite structure of the carbon shell of each formed agglomerate and the carbon bound to oxygen (see Table S6). The W–C and B–C bond fractions range from 2 to 4% and from 17 to 19%, respectively (see Table S6).

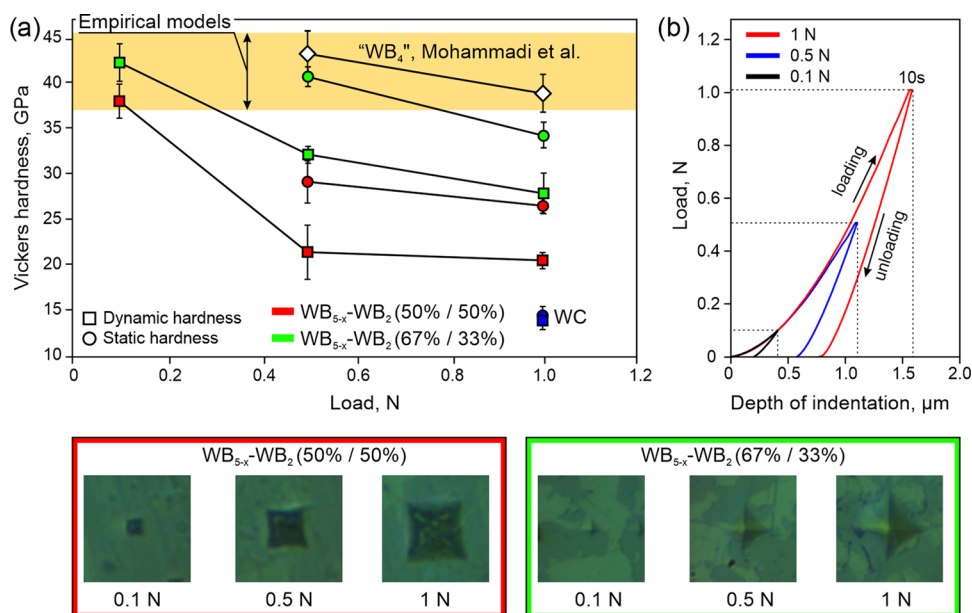


Figure 5. (a) Vickers microhardness of $\text{WB}_{5-x}-\text{WB}_2$ (red and green points are for 50 and 67% of WB_{5-x} in the sample, respectively) and WC (blue points) measured in static (circles) and dynamic (squares) regimes at different loads of 0.1, 0.5, and 1 N in comparison with the microhardness of “ WB_4 ”⁷ (open rhombuses). Orange color shows the range of calculated values for WB_{5-x} obtained for different x using the empirical Mazhnik–Oganov model.⁶⁸ Bottom panels show the indenter imprints at different loads for two types of samples. (b) Typical dependence of load on the depth of indentation obtained from the indentation of a synthesized sample of $\text{WB}_{5-x}-\text{WB}_2$ at maximum loads of 0.1 (black), 0.5 (blue), and 1 N (red).

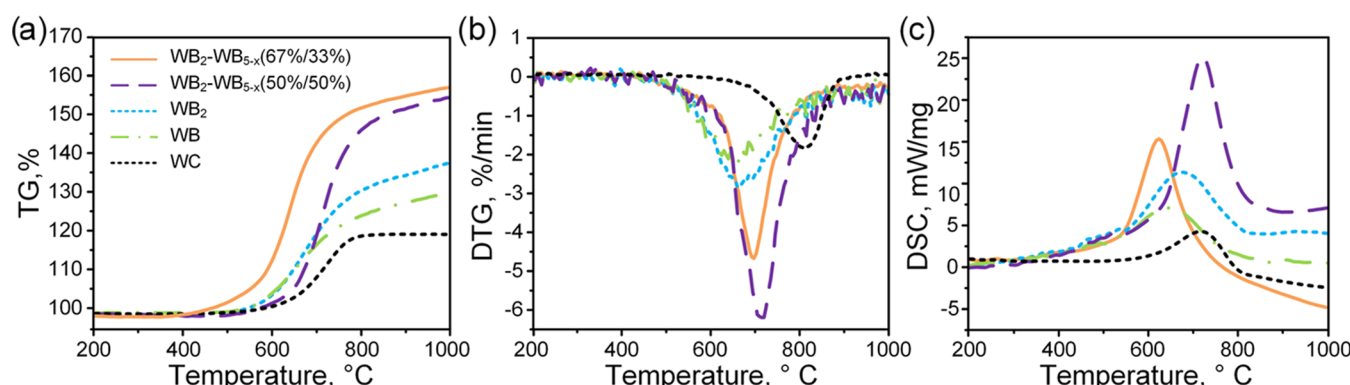


Figure 6. Results of differential thermal analysis of four types of samples based on WB (green), WB_2 (dashed blue), two samples of $\text{WB}_{5-x}-\text{WB}_2$ containing 67 (orange) and 50% (violet) of WB_{5-x} , and commercial WC (solid black). (a) TG curves, (b) derivative thermogravimetry (DTG) curves, and (c) differential scanning calorimetry (DSC) curves.

According to obtained information from the XPS study, we can conclude that despite the presence of carbon in our experimental setup, the tungsten carbide is not formed, and only the formation of boride phases was observed. Thus, we showed that our proposed scheme with vacuumless method is the cheap and efficient way of synthesis of higher tungsten borides with comparable quality to those made by vacuum techniques.

Microhardness Measurements. Higher tungsten boride WB_{5-x} belongs to the class of superhard materials as was shown previously.^{1,3,7} We showed that samples of $\text{WB}_{5-x}-\text{WB}_2$ with different amounts of WB_{5-x} produced by the newly proposed vacuumless technique are hard, as confirmed by performing microhardness measurements that were made at various loads from 0.1 to 1 N, as shown in Figure 5a. The indenter imprints at each load are shown in the bottom panel of Figure 5. One can see that the measured static microhard-

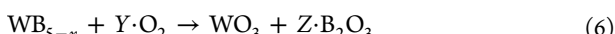
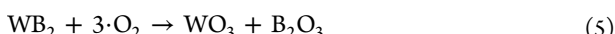
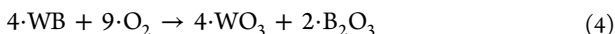
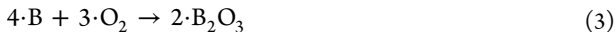
ness for $\text{WB}_{5-x}-\text{WB}_2$ (50/50%) varies from 29.3 ± 2.3 to 26.6 ± 0.5 GPa at loads of 0.5 and 1 N, while the measured static microhardness for $\text{WB}_{5-x}-\text{WB}_2$ (67/33%) varies from 38.7 ± 1.1 to 34.1 ± 2.1 GPa at loads of 0.5 and 1 N. The load-dependent hardness, commonly known as the indentation size effect,⁶⁵ has been observed with several other superhard materials as well.^{7,66,67} In Figure 5b, the typical load curves for the $\text{WB}_{5-x}-\text{WB}_2$ sample with the ratio of $\text{WB}_{5-x}/\text{WB}_2$ equal to 67:33 are shown under applied loads of 0.1, 0.5, and 1 N. One can clearly see the loading and unloading regions at these loads of 0.1, 0.5, and 1 N, where the maximal achieved indentation depths were 0.45, 1.09, and 1.58 μm , respectively.

Measured low-load (0.1 N) Vickers microhardness in the dynamic regime shows values of 38.2 ± 1.8 and 42.1 ± 2.1 GPa (for 50 and 67% of WB_{5-x} in the sample), which are consistent with the hardness calculated by the Mazhnik–Oganov empirical model⁶⁸ (orange color in Figure 5a). A wide

range of calculated values (from 36.6 to 45.2 GPa) is associated with the number of exact compositions that were used for calculations and were taken from ref 3. Our result with a larger amount of WB_{5-x} in the sample slightly differs from that obtained by Mohammadi et al.⁷ and Kvashnin et al.³ due to the difference in sample preparation for hardness testing. Here, we performed indentation of microsized pieces of WB_{5-x} – WB_2 incorporated into the epoxy resin, while in refs 3 and 7, the solid samples of higher tungsten boride were tested.

However, one can see that the microhardness of WC measured within the same framework (average size of this powder was up to 100 μm) and at the same conditions is much lower compared to WB_{5-x} – WB_2 and equal to 13.9 ± 1.1 GPa under an applied load of 1 N (blue points in Figure 5a). The hardness of WC, measured previously^{69,70} at similar conditions, well correspond to our measurements. This proves that the proposed technique for effective and inexpensive synthesis of WB_{5-x} – WB_2 leads to formation of superhard pieces of the material, which are much harder than WC.

Thermogravimetric (TG) Analysis. As the main application of WB_{5-x} – WB_2 is related to the gas and oil industry as a drill bit cutter, it is important for the material to be resistant against oxidation. The results of differential thermogravimetric analysis of the four types of synthesized samples (based on WB, WB_2 , and two WB_{5-x} – WB_2 with different amounts of WB_{5-x}) are shown in Figure 6. As can be seen from the TG curves (Figure 6a), all samples are characterized by a monomodal gain in mass during heating in an oxidizing environment. During the heating process, the weight gain varied from 30 wt % (for WB) up to 55 wt % (for WB_2 + WB_{5-x}). Weight gain is caused by the oxidation processes



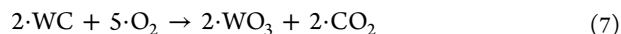
It should be noted that the mass balance during weight gain by the samples might not correspond to the above expressions due to the possible evaporation of tungsten and boron oxides at temperatures above 800–1000 °C. The temperature of the onset of intense oxidation of all samples is in the range of 407–470 °C; the higher temperature of intense oxidation corresponds to the sample with a higher amount of WB_{5-x} (see Table S4 in the Supporting Information).

The extremum of the DTG function (Figure 6b) is in the range from 650 to 720 °C and increases with the boron ratio in the initial mixture, which the studied samples were obtained from. The reaction rate is also higher for samples with a high boron content. The temperature of the maximum rate of the oxidation reaction of obtained samples is at least 650 °C, which is slightly higher in comparison with data from ref 71. It is known that the oxidation temperature can significantly depend on the phase composition of the powders, their dispersion, presence and nature of impurities, and heating dynamics. In addition, it is very difficult to synthesize the pure phase of tungsten boride powders.⁷¹ In ref 16, the temperature of intense oxidation of WB_2 occurs at 750 °C, which is higher than in our work. Possible reasons may be an inaccurate match of the phase composition of the analyzed material and the larger particle size (about 100 μm).¹⁶ Wang et al.⁷² synthesized

samples of higher tungsten boride and showed a higher oxidation temperature of 588 °C compared to our results due to the usage of bulk sintered ceramic samples with larger grains. In ref 73, samples made of WB_2 particles of both micron and submicron range are characterized by the temperature of the maximum oxidation rate of 633 °C.⁷³ At the same time, oxidation was observed in the temperature range from 400 to 790 °C, which is lower than in our work. The reason for higher characteristic temperatures of the burning process of our samples (with comparable parameters of granulometric composition) may be the presence of carbon shells of nanosized particles, which can protect nanosized particles from oxidation.⁷⁴ We can say that oxidation of synthesized samples containing WB_{5-x} and WB_2 phases occurs at lower characteristic temperatures than oxidation of relatively large crystals (bulk bodies, particles with average size of hundreds of micrometers). At the same time, our characteristic temperatures of oxidations are higher than that for submicron and nanoscale tungsten boride crystals.

The higher reaction rate and the specific calorific value of the samples (differential scanning calorimetry (DSC) results, Figure 6c), in which the proportion of boron is higher, may be due to the presence of a certain amount of unbound boron and its intense oxidation.

The characteristics of the oxidation process of the obtained samples require comparison with similar data of known superhard materials. Here, we perform a comparison with the most common material for elements of cutting and drilling tools—WC. We use a commercial tungsten carbide powder (WC) with average particle size up to 100 μm . Oxidation of tungsten carbide takes place according to the well-known exothermic reaction with the release of carbon dioxide



The initial temperature of intense oxidation of WC powder is slightly higher than that of the synthesized tungsten boride samples; the final temperature of intense oxidation T_f is higher for the higher tungsten boride (see Figure 6). The oxidation rate of reaction for the WC sample is lower than for the synthesized samples, which may be due to the presence of unbound boron in the higher tungsten boride samples. The DSC subintegral region for the WC sample is lower (Figure 6c).

Based on obtained data, one can see that the oxidation reaction of commercial tungsten carbide occurs at a lower rate and begins at a temperature ~800 °C higher than that of WB_2 and WB_{5-x} samples. The end temperature of the intensive oxidation process in the WB_{5-x} samples is higher than that of commercial WC. Thus, it can be concluded that the synthesized samples are characterized by similar (in terms of operational characteristics) parameters of the oxidation process with a commercial WC powder. It should be noted that a pure and relatively coarse tungsten carbide powder was used for comparison; the parameters of the oxidation process are significantly influenced by impurities and the average particle size.⁷⁵ In particular, submicron tungsten carbide particles begin to oxidize at ~400 °C.⁷⁴ Nevertheless, the actual results show that the synthesized samples are comparable in oxidation parameters to commercial tungsten carbide, despite the presence of nanosized particles and unbound boron in them, which contribute to the intensification of oxidation processes. X-ray diffraction patterns of studied samples after thermal treatments are shown in Figure S8 in the Supporting

Information. According to the obtained XRD patterns, the major phase after annealing is WO_3 . There are also minor reflections related to the material of the vessels in which the measurements were made. In contrast to WB, WB_2 , and WC, the $\text{WB}_2\text{--WB}_{5-x}$ (67/33%) sample showed additional reflections from graphite, boron oxide (B_2O_3), traces of WB_2 and WB_{5-x} , and calcium tungstate (CaWO_4), as shown in Figure S8.

The proposed approach of vacuumless synthesis of powders of higher tungsten boride allows one to produce materials based on WB_{5-x} with higher oxidation resistance than for WB, WB_2 , and W_2B_5 ⁷⁵ and comparable to commercial WC.⁷⁵ Taking into account the higher mechanical characteristics of the $\text{WB}_{5-x}\text{--WB}_2$ sample, one can conclude that $\text{WB}_{5-x}\text{--WB}_2$ is a very attractive material for practical and even industrial applications and is a worthy competitor to the widespread tungsten carbides today.

CONCLUSIONS

In this research, we proposed a new efficient and inexpensive method toward the synthesis of superhard higher tungsten borides based on the vacuumless direct current arc plasma process. Comprehensive investigation of the synthesis conditions and structure of the obtained materials was performed using experimental (XRD, TEM, SEM, XPS, etc.) and computational techniques. The XRD study showed that the synthesized product contains two boride phases, whose crystal structures, WB_2 and WB_{5-x} , were refined using the DFT calculations. The proposed method allows one to finely adjust the experimental parameters to control the composition of the product. Optimization of experimental parameters leads to an increase in the amount of WB_{5-x} in the sample to 61.5% by volume. Microhardness measurements show that the synthesized powder of $\text{WB}_{5-x}\text{--WB}_2$ is twice harder than WC at the same conditions, while thermogravimetric analysis shows a higher oxidation resistance of the synthesized powder of $\text{WB}_{5-x}\text{--WB}_2$ in comparison to other tungsten borides and to commercial WC. Our method is the first step toward controllable vacuumless large-scale synthesis of superhard WB_{5-x} having intriguing perspectives in industrial applications due to their unique properties. Further study is necessary to improve the presented technique to maximize the ratio of WB_{5-x} in the synthesized samples.

ASSOCIATED CONTENT

Supporting Information

The Supporting Information is available free of charge at <https://pubs.acs.org/doi/10.1021/acs.inorgchem.1c03880>.

Detailed information about crystal data of predicted compounds, calculated convex hull at 2000 K, XRD patterns of WB_2 , W_2B_5 , and WB_{5-x} , SEM of the $\text{WB}_{5-x}\text{--WB}_2$ and WB samples, TEM and HRTEM, SAED data, oxidation process parameters and XRD data after annealing, and XPS measurements (PDF)

AUTHOR INFORMATION

Corresponding Author

Alexander G. Kvashnin – Skolkovo Institute of Science and Technology, Skolkovo Innovation Center, Moscow 121205, Russia; orcid.org/0000-0002-0718-6691; Email: A.Kvashnin@skoltech.ru

Authors

Alexander Ya. Pak – National Research Tomsk Polytechnic University, Tomsk 634050, Russia
Dmitry V. Rybkovskiy – Skolkovo Institute of Science and Technology, Skolkovo Innovation Center, Moscow 121205, Russia; orcid.org/0000-0002-5938-4542
Yuliya Z. Vassilyeva – National Research Tomsk Polytechnic University, Tomsk 634050, Russia
Ekaterina N. Kolobova – National Research Tomsk Polytechnic University, Tomsk 634050, Russia
Alexander V. Filimonenko – National Research Tomsk Polytechnic University, Tomsk 634050, Russia

Complete contact information is available at: <https://pubs.acs.org/10.1021/acs.inorgchem.1c03880>

Notes

The authors declare no competing financial interest.

ACKNOWLEDGMENTS

A.G.K. and D.V.R. thank the Russian Science Foundation (grant no. 19-72-30043). The calculations were carried out on the Arkuda supercomputer of the Skolkovo Foundation. A.Y.P. and Y.Z.V. thank the Tomsk Polytechnic University development program (DC arc plasma reactor system's automation). The authors thank the central laboratories of TPU (Analytical Center) for the XPS measurements. We also thank Igor Grishin (Skoltech) for proofreading the manuscript.

REFERENCES

- (1) Kvashnin, A. G.; Zakaryan, H. A.; Zhao, C.; Duan, Y.; Kvashnina, Y. A.; Xie, C.; Dong, H.; Oganov, A. R. New Tungsten Borides, Their Stability and Outstanding Mechanical Properties. *J. Phys. Chem. Lett.* **2018**, *9*, 3470–3477.
- (2) Cheng, X.-Y.; Chen, X.-Q.; Li, D.-Z.; Li, Y.-Y. Computational Materials Discovery: The Case of the W–B System. *Acta Crystallogr., Sect. C: Struct. Chem.* **2014**, *70*, 85–103.
- (3) Kvashnin, A. G.; Rybkovskiy, D. V.; Filonenko, V. P.; Bugakov, V. I.; Zibrov, I. P.; Brazhkin, V. V.; Oganov, A. R.; Osipov, A. A.; Zakirov, A. Y. WB_{5-x} : Synthesis, Properties, and Crystal Structure. New Insights Into the Long-Debated Compound. *Adv. Sci.* **2020**, *7*, No. 200775.
- (4) Szwacki, N. G. The Structure and Hardness of the Highest Boride of Tungsten, a Borophene-Based Compound. *Sci. Rep.* **2017**, *7*, No. 4082.
- (5) Chrzanowska-Giżyńska, J.; Denis, P.; Woźniacka, S.; Kurpaska, Ł. Mechanical Properties and Thermal Stability of Tungsten Boride Films Deposited by Radio Frequency Magnetron Sputtering. *Ceram. Int.* **2018**, *44*, 19603–19611.
- (6) Chong, X.; Jiang, Y.; Zhou, R.; Feng, J. Stability, Chemical Bonding Behavior, Elastic Properties and Lattice Thermal Conductivity of Molybdenum and Tungsten Borides under Hydrostatic Pressure. *Ceram. Int.* **2016**, *42*, 2117–2132.
- (7) Mohammadi, R.; Lech, A. T.; Xie, M.; Weaver, B. E.; Yeung, M. T.; Tolbert, S. H.; Kaner, R. B. Tungsten Tetraboride, an Inexpensive Superhard Material. *Proc. Natl. Acad. Sci. U.S.A.* **2011**, *108*, 10958–10962.
- (8) Li, Q.; Wang, L.; Ai, X.; Chen, H.; Zou, J.; Li, G.-D.; Zou, X. Multiple Crystal Phases of Intermetallic Tungsten Borides and Phase-Dependent Electrocatalytic Property for Hydrogen Evolution. *Chem. Commun.* **2020**, *56*, 13983–13986.
- (9) Chen, Y.; Ye, Y.; Tao, Q.; Yang, L.; Cheng, J.; Liu, X.; Cao, J.; Fan, H.; Wei, M.; Zhu, P.; Yang, L.; Yang, J. Constructing 1D Boron Chains in the Structure of Transition Metal Monoborides for Hydrogen Evolution Reactions. *Catalysts* **2021**, *11*, No. 1265.

- (10) Wang, A.; Shen, L.; Zhao, M.; Wang, J.; Zhou, W.; Li, W.; Feng, Y.; Liu, H. Tungsten Boride: A 2D Multiple Dirac Semimetal for the Hydrogen Evolution Reaction. *J. Mater. Chem. C* **2019**, *7*, 8868–8873.
- (11) Itoh, H.; Matsudaira, T.; Naka, S.; Hamamoto, H.; Obayashi, M. Formation Process of Tungsten Borides by Solid State Reaction between Tungsten and Amorphous Boron. *J. Mater. Sci.* **1987**, *22*, 2811–2815.
- (12) Frotscher, M.; Klein, W.; Bauer, J.; Fang, C.-M.; Halet, J.-F.; Senyshyn, A.; Baehtz, C.; Albert, B. M_2B_3 or M_3B_4 ? A Reinvestigation of the Mo/B and W/B System. *Z. Anorg. Allg. Chem.* **2007**, *633*, 2626–2630.
- (13) Zhao, C.; Duan, Y.; Gao, J.; Liu, W.; Dong, H.; Dong, H.; Zhang, D.; Oganov, A. R. Unexpected Stable Phases of Tungsten Borides. *Phys. Chem. Chem. Phys.* **2018**, *20*, 24665–24670.
- (14) Veblen, D. R. Polysomatism and Polysomatic Series: A Review and Applications. *Am. Mineralogist* **1991**, *76*, 801–826.
- (15) Kiessling, R.; Wetterholm, A.; Sillén, L. G.; et al. The Crystal Structures of Molybdenum and Tungsten Borides. *Acta Chem. Scand.* **1947**, *1*, 893–916.
- (16) Okada, S.; Kudou, K.; Lundström, T. Preparations and Some Properties of W_2B , δ -WB and WB₂ Crystals from High-Temperature Metal Solutions. *Jpn. J. Appl. Phys.* **1995**, *34*, 226.
- (17) Woods, H. P.; Wawner, F. E.; Fox, B. G. Tungsten Diboride: Preparation and Structure. *Science* **1966**, *151*, 75.
- (18) Chretien, A.; Helcrosky, J. Sur Les Borones de Molybdone et de Tungstene MoB_4 , et WB₄, Composes Nouveaux. *C. R. Hebd. Séances Acad. Sci.* **1961**, *252*, 742–744.
- (19) Gu, Q.; Krauss, G.; Steurer, W. Transition Metal Borides: Superhard versus Ultra-Incompressible. *Adv. Mater.* **2008**, *20*, 3620–3626.
- (20) Romans, P. A.; Krug, M. P. Composition and Crystallographic Data for the Highest Boride of Tungsten. *Acta Crystallogr.* **1966**, *20*, 313–315.
- (21) Nowotny, H.; Haschke, H.; Benesovsky, F. Bor-reiche Wolframboride. *Monatsh. Chem.—Chem. Mon.* **1967**, *98*, 547–554.
- (22) Rudy, E.; Benesovsky, F.; Toth, L. Untersuchung Der Dreistoffsysteme Der Va-Und VIa-* Metalle Mit Bor Und Kohlenstoff. *Int. J. Mater. Res.* **1963**, *54*, 345–353.
- (23) Lundström, T.; Rosenberg, I. The Crystal Structure of the Molybdenum Boride $Mo_{1-x}B_3$. *J. Solid State Chem.* **1973**, *6*, 299–305.
- (24) Zeiringer, I.; Rogl, P.; Grytsiv, A.; Polt, J.; Bauer, E.; Giester, G. Crystal Structure of $W_{1-x}B_3$ and Phase Equilibria in the Boron-Rich Part of the Systems Mo-Rh-B and W-{Ru,Os,Rh,Ir,Ni,Pd,Pt}-B. *J. Phase Equilif. Diffus.* **2014**, *35*, 384–395.
- (25) Lech, A. T.; Turner, C. L.; Mohammadi, R.; Tolbert, S. H.; Kaner, R. B. Structure of Superhard Tungsten Tetraboride: A Missing Link between MB₂ and MB₁₂ Higher Borides. *Proc. Natl. Acad. Sci. U.S.A.* **2015**, *112*, 3223–3228.
- (26) Garbiec, D.; Wiśniewska, M.; Psiuk, R.; Denis, P.; Leviant-Zayonts, N.; Leshchynsky, V.; Rubach, R.; Mościcki, T. Zirconium Alloyed Tungsten Borides Synthesized by Spark Plasma Sintering. *Arch. Civ. Mech. Eng.* **2021**, *21*, No. 37.
- (27) Pak, A. Y.; Shanenkov, I. I.; Mamontov, G. Y.; Kokorina, A. I. Vacuumless Synthesis of Tungsten Carbide in a Self-Shielding Atmospheric Plasma of DC Arc Discharge. *Int. J. Refract. Met. Hard Mater.* **2020**, *93*, No. 105343.
- (28) Pak, A.; Ivashutenko, A.; Zakharova, A.; Vassilyeva, Y. Cubic SiC Nanowire Synthesis by DC Arc Discharge under Ambient Air Conditions. *Surf. Coat. Technol.* **2020**, *387*, No. 125554.
- (29) Pak, A. Y.; Vassilyeva, Y. Z. Device for Producing Tungsten Carbide-Based Powders. RU191334U1, Aug 1, 2019.
- (30) Gerasimov, R. D.; Vassilyeva, Y. Z.; Pak, A. Y. Control and Monitoring of Operating Cycle Parameters of a Biaxial Electric Arc Reactor in Automatic and Manual Modes. RU2021662706, Aug 3, 2021.
- (31) Takeshi, E.; Billinge, S. J. L. Crystallographic Analysis of Complex Materials. In *Underneath the Bragg Peaks Structural Analysis of Complex Materials*, Egami, T.; Billinge, S. J. L., Eds.; Pergamon Materials Series; Pergamon, 2012; Chapter 2, Vol. 16, pp 27–54.
- (32) Snyder, R. L. The Use of Reference Intensity Ratios in X-ray Quantitative Analysis. *Powder Diffr.* **1992**, *7*, 186–193.
- (33) Hubbard, C. R.; Snyder, R. L. RIR - Measurement and Use in Quantitative XRD. *Powder Diffr.* **1988**, *3*, 74–77.
- (34) Hohenberg, P.; Kohn, W. Inhomogeneous Electron Gas. *Phys. Rev.* **1964**, *136*, B864–B871.
- (35) Kohn, W.; Sham, L. J. Self-Consistent Equations Including Exchange and Correlation Effects. *Phys. Rev.* **1965**, *140*, A1133–A1138.
- (36) Perdew, J. P.; Burke, K.; Ernzerhof, M. Generalized Gradient Approximation Made Simple. *Phys. Rev. Lett.* **1996**, *77*, 3865–3868.
- (37) Blöchl, P. E. Projector Augmented-Wave Method. *Phys. Rev. B* **1994**, *50*, 17953–17979.
- (38) Kresse, G.; Joubert, D. From Ultrasoft Pseudopotentials to the Projector Augmented-Wave Method. *Phys. Rev. B* **1999**, *59*, 1758–1775.
- (39) Kresse, G.; Hafner, J. Ab Initio Molecular Dynamics for Liquid Metals. *Phys. Rev. B* **1993**, *47*, 558–561.
- (40) Kresse, G.; Hafner, J. Ab Initio Molecular-Dynamics Simulation of the Liquid-Metal-Amorphous-Semiconductor Transition in Germanium. *Phys. Rev. B* **1994**, *49*, 14251–14269.
- (41) Kresse, G.; Furthmüller, J. Efficient Iterative Schemes for Ab Initio Total-Energy Calculations Using a Plane-Wave Basis Set. *Phys. Rev. B* **1996**, *54*, 11169–11186.
- (42) Methfessel, M.; Paxton, A. T. High-Precision Sampling for Brillouin-Zone Integration in Metals. *Phys. Rev. B* **1989**, *40*, 3616–3621.
- (43) Kern, G.; Kresse, G.; Hafner, J. Ab Initio Calculation of the Lattice Dynamics and Phase Diagram of Boron Nitride. *Phys. Rev. B* **1999**, *59*, 8551–8559.
- (44) Togo, A.; Tanaka, I. First Principles Phonon Calculations in Materials Science. *Scr. Mater.* **2015**, *108*, 1–5.
- (45) Togo, A.; Oba, F.; Tanaka, I. First-Principles Calculations of the Ferroelastic Transition between Rutile-Type and CaCl₂-Type SiO₂ at High Pressures. *Phys. Rev. B* **2008**, *78*, No. 134106.
- (46) Oganov, A. R.; Glass, C. W. Crystal Structure Prediction Using Ab Initio Evolutionary Techniques: Principles and Applications. *J. Chem. Phys.* **2006**, *124*, No. 244704.
- (47) Oganov, A. R.; Ma, Y.; Lyakhov, A. O.; Valle, M.; Gatti, C. Evolutionary Crystal Structure Prediction as a Method for the Discovery of Minerals and Materials. *Rev. Miner. Geochem.* **2010**, *71*, 271–298.
- (48) Oganov, A. R.; Lyakhov, A. O.; Valle, M. How Evolutionary Crystal Structure Prediction Works—and Why. *Acc. Chem. Res.* **2011**, *44*, 227–237.
- (49) Lyakhov, A. O.; Oganov, A. R.; Stokes, H. T.; Zhu, Q. New Developments in Evolutionary Structure Prediction Algorithm USPEX. *Comput. Phys. Commun.* **2013**, *184*, 1172–1182.
- (50) Bushlanov, P. V.; Blatov, V. A.; Oganov, A. R. Topology-Based Crystal Structure Generator. *Comput. Phys. Commun.* **2019**, *236*, 1–7.
- (51) Li, Q.; Zhou, D.; Zheng, W.; Ma, Y.; Chen, C. Global Structural Optimization of Tungsten Borides. *Phys. Rev. Lett.* **2013**, *110*, No. 136403.
- (52) Colton, R. J.; Rabalais, J. W. Electronic Structure to Tungsten and Some of Its Borides, Carbides, Nitrides, and Oxides by x-Ray Electron Spectroscopy. *Inorg. Chem.* **1976**, *15*, 236–238.
- (53) Rahimnejad, S.; He, J. H.; Pan, F.; Lee, X.; Chen, W.; Wu, K.; Xu, G. Q. Enhancement of the Photocatalytic Efficiency of WO₃ nanoparticles via Hydrogen Plasma Treatment. *Mater. Res. Express* **2014**, *1*, No. 045044.
- (54) Jiang, C.; Pei, Z.; Liu, Y.; Xiao, J.; Gong, J.; Sun, C. Preparation and Characterization of Superhard AlB₂-Type WB₂ Nanocomposite Coatings. *Phys. Status Solidi A* **2013**, *210*, 1221–1227.
- (55) Tao, Q.; Zheng, D.; Zhao, X.; Chen, Y.; Li, Q.; Li, Q.; Wang, C.; Cui, T.; Ma, Y.; Wang, X.; Zhu, P. Exploring Hardness and the Distorted sp² Hybridization of B–B Bonds in WB₃. *Chem. Mater.* **2014**, *26*, 5297–5302.
- (56) Magnusson, M.; Tengdelius, L.; Eriksson, F.; Samuelsson, M.; Broitman, E.; Greczynski, G.; Hultman, L.; Höglberg, H. Reactive

- Magnetron Sputtering of Tungsten Target in Krypton/Trimethylboron Atmosphere. *Thin Solid Films* **2019**, *688*, No. 137384.
- (57) Wang, H.; Yan, X.; Zhang, H.; Gee, M.; Zhao, C.; Liu, X.; Song, X. Oxidation-Dominated Wear Behaviors of Carbide-Based Cermet: A Comparison between WC-WB-Co and Cr₃C₂-NiCr Coatings. *Ceram. Int.* **2019**, *45*, 21293–21307.
- (58) Pan, J.; Zhen, C.; Wang, L.; Liu, G.; Cheng, H.-M. WB Crystals with Oxidized Surface as Counter Electrode in Dye-Sensitized Solar Cells. *Sci. Bull.* **2017**, *62*, 114–118.
- (59) Zhao, F.; Qiu, L.; Ding, Z.; Li, Y.; Yao, B.; Shen, W.; Li, Q.; Zhu, P. Synthesis and Characterization of WB₂-WB₃-B₄C Hard Composites. *Int. J. Refract. Met. Hard Mater.* **2019**, *82*, 268–272.
- (60) Guo, F.; Wu, Y.; Ai, X.; Chen, H.; Li, G.-D.; Chen, W.; Zou, X. A Class of Metal Diboride Electrocatalysts Synthesized by a Molten Salt-Assisted Reaction for the Hydrogen Evolution Reaction. *Chem. Commun.* **2019**, *55*, 8627–8630.
- (61) He, D.; Shang, L.; Lu, Z.; Zhang, G.; Wang, L.; Xue, Q. Tailoring the Mechanical and Tribological Properties of B₄C/a-C Coatings by Controlling the Boron Carbide Content. *Surf. Coat. Technol.* **2017**, *329*, 11–18.
- (62) Chen, R.; Su, L.; Qi, J.; Shi, Q.; Shi, Y.; Liao, Z.; Lu, T. Effect of Deposition Time on the Growth Mode and Stoichiometric of Amorphous Boron Carbide Thin Films Deposited by Electron Beam Evaporation. *Ceram. Int.* **2018**, *44*, 17298–17304.
- (63) Dash, T.; Nayak, B. B. Preparation of Multi-Phase Composite of Tungsten Carbide, Tungsten Boride and Carbon by Arc Plasma Melting: Characterization of Melt-Cast Product. *Ceram. Int.* **2016**, *42*, 445–459.
- (64) Dash, T.; Nayak, B. B.; Abhangi, M.; Makwana, R.; Vala, S.; Jakhar, S.; Rao, C. V. S.; Basu, T. K. Preparation and Neutronic Studies of Tungsten Carbide Composite. *Fusion Sci. Technol.* **2014**, *65*, 241–247.
- (65) Nix, W. D.; Gao, H. Indentation Size Effects in Crystalline Materials: A Law for Strain Gradient Plasticity. *J. Mech. Phys. Solids* **1998**, *46*, 411–425.
- (66) Chung, H.-Y.; Yang, J.-M.; Tolbert, S. H.; Kaner, R. B. Anisotropic Mechanical Properties of Ultra-Incompressible, Hard Osmium Diboride. *J. Mater. Res.* **2008**, *23*, 1797–1801.
- (67) Chung, H.-Y.; Weinberger, M. B.; Levine, J. B.; Kavner, A.; Yang, J.-M.; Tolbert, S. H.; Kaner, R. B. Synthesis of Ultra-Incompressible Superhard Rhenium Diboride at Ambient Pressure. *Science* **2007**, *316*, 436–439.
- (68) Mazhnik, E.; Oganov, A. R. A Model of Hardness and Fracture Toughness of Solids. *J. Appl. Phys.* **2019**, *126*, No. 125109.
- (69) Csanádi, T.; Bl'anda, M.; Chinh, N. Q.; Hvízdos, P.; Dusza, J. Orientation-Dependent Hardness and Nanoindentation-Induced Deformation Mechanisms of WC Crystals. *Acta Mater.* **2015**, *83*, 397–407.
- (70) Schrottner, H.; Kurlov, A. S.; Leenaers, A.; van den Berghe, S.; et al. Microstructure of Nanocrystalline Wc Powders and Wc-Co Hard Alloys. *Rev. Adv. Mater. Sci.* **2011**, *27*, 165–172.
- (71) Dai, B.; Ding, X.; Deng, X.; Zhu, J.; Ran, S. Synthesis of W2B5 Powders by the Reaction between WO₃ and Amorphous B in NaCl/KCl Flux. *Ceram. Int.* **2020**, *46*, 14469–14473.
- (72) Wang, W.; Peng, F.; Liang, H.; Guan, S.; Liang, W.; Zhang, L.; Huang, M.; Tang, Y.; He, D. Synthesis and Sintering of Tungsten Tetraboride and Tantalum-Bearing Tungsten Tetraboride under Ultra High Temperature and High Pressure. *Int. J. Refract. Met. Hard Mater.* **2022**, *102*, No. 105701.
- (73) Ma, K.; Xue, X.; Cao, X. Low-Temperature Synthesis of Tungsten Diboride Powders via a Simple Molten Salt Route. *Int. J. Appl. Ceram. Technol.* **2020**, *17*, 1177–1182.
- (74) Shanenkov, I.; Nikitin, D.; Ivashutenko, A.; Shanenkova, Y.; Vympina, Y.; Butenko, D.; Han, W.; Sivkov, A. Studies on the Thermal Stability of Nanosized Powder of WC_{1-x}-Based Product Prepared by Plasma Dynamic Method, Compaction Feasibility of the Powder and Preparation of Composite with Aluminium. *Ceram. Int.* **2021**, *47*, 6884–6895.
- (75) Kurlov, A. S.; Gusev, A. I. Oxidation of Tungsten Carbide Powders in Air. *Int. J. Refract. Met. Hard Mater.* **2013**, *41*, 300–307.